Journal of Materials Chemistry C

Synergistic Effects of Pd Single Atoms and Nanoclusters Boosting SnO2 Gas Sensing Performance

Journal:	*Journal of Materials Chemistry C*
Manuscript ID	TC-ART-11-2024-004761.R1
Article Type:	Paper
Date Submitted by the Author:	20-Jan-2025
Complete List of Authors:	OZBAKIR, YAPRAK; University of California Berkeley, Chemical and Biomolecular Engineering Xia, Yong ; Xi'an Jiaotong University, Manufacturing Systems Engineering Pan, Aifei; Xi'an Jiaotong University, Manufacturing Systems Engineering Hong, Jiyun; SLAC National Accelerator Laboratory Perez-Aguilar, Jorge; SLAC National Accelerator Laboratory Bare, Simon; SLAC National Accelerator Laboratory, SSRL Rossi, Francesca; IMEM CNR, Dhall , Rohan; Lawrence Berkeley Laboratory, The National Center for Electron Microscopy (NCEM) Ali Alghannam, Afnan; University of California Berkeley, Chemical and Biomolecular Engineering Goel, Nishit; InvenSense Inc Bart, Stephen; InvenSense Inc Carraro, Carlo; University of California Berkeley College of Chemistry, Maboudian, Roya; University of California Berkeley, Chemical and Biomolecular Engineering

ARTICLE

Synergistic Effects of Pd Single Atoms and Nanoclusters Boosting SnO_2 Gas Sensing Performance

Received 00th January 20xx,
Accepted 00th January 20xx

DOI: 10.1039/x0xx00000x

Yaprak Ozbakir [a, b], Yong Xia [c, d], Aifei Pan [d], Jiyun Hong [e], Jorge E. Perez-Aguilar [e], Simon R. Bare [e], Francesca Rossi [f], Rohan Dhall [g], Afnan Ali Alghannam [a], Nishit Goel [h], Stephen Bart [h], Carlo Carraro [a, b], and Roya Maboudian [a, b, *]

Tin (IV) oxide-supported Pd is a promising heterogenous catalyst for CO oxidation relevant for environmental cleanup reactions. In this study, atomically dispersed catalyst Pd on SnO_2 (ADC Pd/SnO_2) hybrid material is successfully synthesized *via* a straightforward wet chemistry method and is found to exhibit superior performance toward CO sensing. *Ex-situ* EXAFS analysis confirms the formation of single Pd atoms and small Pd nanoclusters stabilized on the SnO_2(110) surface. The material exhibits high efficiency in generating adsorbed O_2^- as well as high activity in catalyzing CO oxidation at low temperatures, resulting in exceptional sensitivity and selectivity toward CO in comparison to pure SnO_2 and Pd nanoparticles loaded on SnO_2 respectively. *In-situ* FTIR measurements unravel CO adsorption kinetics on ADC Pd/SnO_2 under reaction conditions, and a possible sensing mechanism is put forth in which CO is transformed into CO_2 by reaction with active oxygen species; and concurrently, carbon-related species (bicarbonates and carbonates) are formed and decomposed into CO_2.

Introduction

On average, an adult, moderately active during the daytime, breathes 20,000 times a day, and inevitably, air quality of the environment has a direct impact on human health [1, 2]. Poor air quality causes acute and chronic health problems, including respiratory diseases, heart disease, cognitive deficits, and cancer [3, 4]. Both short- and long-term exposure to high concentrations of air pollutants can cause acute poisoning, which may be fatal [5]. Therefore, it is essential to monitor and assess air quality for human health protection [6]. Carbon monoxide (CO) is one of the main air pollutants that pose serious threats to human health, and thus, requires close monitoring [5]. The threshold limit value – 8-hour time-weighted average (TLV-TWA) and the threshold limit value-ceiling (TLV-Cs) of CO that the Occupational Safety and Health Administration (OSHA) recommendations are 35-200 ppm [7]. This requires realizing real-time gas sensors with high sensitivity and selectivity for detection of gases like CO [2].

Chemiresistive gas sensors, operating based on changes in electrical resistance of a sensing material in response to a given chemical environment by gas surface chemisorption or surface redox reactions, have attracted a great deal of attention owing to their flexibility in fabrication, simplicity, miniaturization, low power consumption, low cost as well as high sensitivity [8, 9]. Semiconductor metal oxides (MOXs), typical sensing materials in chemiresistive gas sensors, require high working temperatures (normally > 250 °C) to provide sufficient activation energy to facilitate oxygen adsorption, and concurrently to stimulate generation of active oxygen species (O_2^-, O^-, and O^{2-}) for the surface reactions [10, 11]. However, at high temperatures, these oxygen species are highly active and can randomly react with the adsorbed gaseous analyte, resulting in the poor selectivity of MOXs. Furthermore, high operating temperature increases energy consumption, raises ignition risk in detection of flammable gases and complicates device fabrication [12, 13].

[a] *Department of Chemical and Biomolecular Engineering, University of California, Berkeley, CA 94720, United States*
[b] *Berkeley Sensor & Actuator Center, Berkeley, CA 94720, United States*
[c] *School of Instrument Science and Technology, Xi'an Jiaotong University, Xi'an 710049, China*
[d] *State Key Laboratory for Manufacturing Systems Engineering, and International Joint Laboratory for Micro/Nano Manufacturing and Measurement Technologies, Xi'an Jiaotong University, Xi'an, 710049, China*
[d] *State Key Laboratory for Manufacturing Systems Engineering, and International Joint Laboratory for Micro/Nano Manufacturing and Measurement Technologies, Xi'an Jiaotong University, Xi'an, 710049, China*
[e] *SSRL, SLAC National Accelerator Laboratory, Menlo Park, California 94025, U.S.A.*
[f] *IMEM-CNR Institute, 43124 Parma, Italy*
[g] *National Center for Electron Microscopy (NCEM), Lawrence Berkeley National Laboratory, Berkeley, CA 94720, U.S.A.*
[h] *TDK InvenSense Inc., San Jose, California 95110, U.S.A.*
*Corresponding author email: maboudia@berkeley.edu
Supplementary Information available: [details of any supplementary information available should be included here]. See DOI: 10.1039/x0xx00000x

Incorporation of noble metals into chemiresistive gas sensors has been proven to be an effective strategy to enhance their sensitivity and selectivity since noble metals are the catalysts for the selective oxidation of the reductive gas by the adsorbed oxygen on MOXs [7, 12, 14, 15]. Nevertheless, noble metal nanoparticles (NPs) are prone to poisoning, resulting in catalyst deactivation [16, 17], limiting long-term stability of chemiresistive gas sensors. In addition, metal NPs usually have relatively low catalytic activity at low temperatures, and different crystal facets of metal NPs, synergetic effect from neighboring metal atoms, and inhomogeneous distribution of metal atoms in NPs result in multiple catalytically active sites, which can simultaneously activate various analytes and decrease their selectivity [15, 18].

Atomically dispersed supported metal catalysts (ADCs), which constitute a new class of materials that contain isolated individual atoms or synergistically coupled few-atom ensembles dispersed on appropriate solid supports [19-24] have gained tremendous attention as a new frontier in heterogeneous catalysis in recent years, and have shown a broad range of applications including electrocatalytic hydrogen evolution reactions [25, 26], electrocatalytic oxygen reduction reactions [27, 28], and water-gas shift reactions [29, 30]. The identical active sites of ADCs enable them to selectively catalyze only a certain kind of reaction. Since all atoms in ADCs are exposed to reactants, and each atom is able to participate in catalytic reactions, instead of being buried and wasted inside nanoparticles, their metal atom utilization efficiency reaches the theoretical maximum of 100%, which can increase the catalytic activity per atom and decrease the metal resources consumption [23, 31-33]. Furthermore, ADCs exhibit modified metal-reaction species interactions and reaction pathways to conventional nanoparticle catalysts consisting of several hundreds of atoms [34-36]. The spatial isolation of the metal atoms in ADCs can further enable them to change the adsorption mode of reactive intermediates and prevent side reactions, which need adjacent metal sites to proceed [35, 37-39].

Chemiresistive gas sensing based on MOX relies on heterogeneous catalysis processes [14, 40]; therefore, unique structural traits, mainly well-defined metal active sites and coordination environment, boosted catalytic activities and tunable selectivity of ADCs have also made them suitable candidates for this type of gas sensor [35, 36]. In addition, a large number of defect sites (steps, corners, vacancies) on metal oxide surface can effectively capture the introduced metal species. The strong interactions between the oxide support and isolated atoms contribute to the stability and catalysis efficiency toward the target gas. Although ADCs exhibit exceptional potential in gas sensing with significant opportunities lying ahead, their use in gas sensing applications is in its early stages [7, 40-42].

In this work, tin (IV) oxide (SnO_2) was selected as a semiconductor support material for gas sensing since it enables ready and reversible release of oxygen in the presence of target gas molecules, and its resistance changes before and after the gas molecule's adsorption [43]. Pd was chosen as the catalyst because of its high activity and outstanding sensitivity toward CO at low temperatures, below 200 °C [44-48]. In particular, an atomically dispersed Pd-loaded SnO_2 (ADC Pd/SnO_2) nano-powder was successfully synthesized *via* a straightforward wet chemistry route. After structurally and chemically characterizing the material, it was integrated into a chemiresistive sensing platform and was found to exhibit exceptional sensitivity and selectivity toward CO compared to pure SnO_2 and Pd nanoparticle on SnO_2 respectively. *Ex-situ* EXAFS analyses revealed that Pd atoms are stabilized on SnO_2(110) surface in the form of single atoms and small Pd nanoclusters. The atomically dispersed Pd^{2+} ions, bound to surface oxygen atoms on the SnO_2, can achieve high efficiency in generating adsorbed O_2^- and high activity for CO oxidation at low temperatures. *In-situ* FTIR measurements unraveled CO surface adsorption on ADC Pd/SnO_2 under reaction conditions and the possible sensing mechanism in which CO is transformed into CO_2 through reactions with active oxygen species, and concurrently, carbon-related species (bicarbonates and carbonates) are formed and decompose into CO_2.

Experimental

Materials and Methods

Chemicals

Palladium (II) acetate ($Pd(OAc)_2$, 98%), palladium(II) chloride ($PdCl_2$, 99%), sodium borohydride ($NaBH_4$, 99.9%), hydrochloric acid solution (37%), toluene (99.8%, anhydrous) and hexane (≥ 95%) were purchased from Sigma-Aldrich. Tin (IV) oxide nano powder (99.9%) was purchased from Inframat® Advanced Materials. Ethanol (≥ 99.9%), isopropyl alcohol (99.9%) and acetone (≥ 99%) were purchased from Merck Milipore. All aqueous solutions were prepared using Mili-Q water (18.2 MΩ).

Preparation of atomically dispersed Pd on SnO_2

ADC Pd/SnO_2 was prepared by a simple wet impregnation method at room temperature using $Pd(OAc)_2$ as the Pd precursor and phase-pure tin (IV) oxide nano powder as the support material (Scheme 1). $Pd(OAc)_2$ contains pure organic ligands that are removable under relatively mild conditions [49]. The FTIR spectrum of the prepared sample (Figure S1) did not show C=O and C–H vibrations of the acetate groups, which

indicates complete removal of ligands. The synthesized catalyst with 0.75 wt % nominal loading was denoted as ADC Pd/SnO_2. First, $Pd(OAc)_2$ (7.97 mg), the Pd precursor, was dissolved in 15 ml anhydrous toluene under an inert atmosphere to form a clear solution. Then, 0.5 g SnO_2, previously annealed in ambient air at 500 °C, was added to the anhydrous toluene solution of $Pd(OAc)_2$ and stirred under an inert atmosphere overnight at 25 °C, yielding a light gray, air-stable material, with the empirical formula (-SnO_x)$Pd(OAc)_2$. The actual Pd loading, comparable to the nominal Pd loading (0.75 wt%), achieved under these conditions suggests that there is a sufficient number of specific surface sites on the SnO_2 for the reaction at 25 °C with $Pd(OAc)_2$. The Pd/SnO_2 catalyst was filtered in open air and washed three times with anhydrous toluene, followed by extensive washing with hexane. Next, the sample was dried under dynamic vacuum at 25 °C overnight and annealed in ambient air at 325 °C to remove the ligands from the metal sites. The samples changed color from light gray to tan, most likely indicative of the formation of PdO [50, 51]. For comparison, Pd nanoparticles loaded onto SnO_2, labeled as Pd NPs/SnO_2, were also synthesized, as detailed in Scheme S1.

Materials characterization

The crystalline structure and phase purity were determined using a Rigaku Miniflex 6G X-ray powder diffractometer with Cu K-alpha radiation (λ = 1.5418 Å). The voltage and current were 40 kV and 15 mA, respectively. The actual Pd loading on the SnO_2 support was measured using inductively coupled plasma optical emission spectroscopy (ICP-OES). The sizes and morphology of the SnO_2 support, ADC Pd/SnO_2, and Pd NPs/SnO_2 were analyzed on a field emission scanning electron microscope (FESEM, Zeiss Gemini Ultra-55) and high-resolution transmission electron microscopy (HRTEM, JEOL 2100-F). To prepare the samples of TEM analysis, the metal oxide powder was dispersed in ethanol followed by drop coating the mixture and drying on holey carbon-coated copper grid.

The surface properties and valence band (VB) spectra of the catalysts were analyzed by X-ray photoelectron spectroscopy (XPS, Omicron) using an Al K_α source. Raman spectroscopy measurements were conducted at room temperature on a Horiba LabRAM confocal Raman spectrometer with an excitation laser of 632.8 nm. The diffuse reflectance UV-VIS spectra were recorded using Agilent Cary 5000 UV-Vis-NIR spectrometer, equipped with an integrating sphere. The measurements were carried out at room temperature in the range 750-200 nm. The diffuse reflectance data were converted into the Kubelka-Munk function, F(R), and Tauc's plots were generated to estimate the band gap energy. The nitrogen adsorption/desorption measurement was performed using Micromeritics ASAP2020 gas-sorption system. About 180 mg of SnO_2 support pre-annealed at 500 °C was degassed at 300 °C overnight prior to the analysis. The dispersion of Pd was characterized by high-angle annular dark field scanning transmission electron microscopy (HAADF-STEM, FEI ThemIS). Samples for TEM were dispersed in ethanol by ultrasonication, and the resulting solution was drop-cast onto carbon films supported on copper grids.

The X-ray absorption spectroscopy (XAS) was used to probe the local electronic and geometric structure around the Pd atoms in the samples. The measurement was performed at Pd K-edge at beamline 9-3 of Stanford Synchrotron Radiation Lightsource (SSRL) at SLAC National Laboratory. Beamline 9-3 is a 16-pole, 2-tesla wiggler beamline with a vertically collimating mirror for harmonic rejection and a cylindrically bent mirror for focusing. The photon energy was selected using a liquid-nitrogen cooled, double-crystal Si (220) monochromator (crystal orientation = 0°). About 40-46 mg of powder was pressed into a 7-mm diameter pellet for both ADC Pd/SnO_2 and Pd NPs/SnO_2. The XAS data were collected in fluorescence yield mode using a PIPS detector perpendicular (90°) to the incident beam with a Soller slit. A total of 9 scans were collected to improve the signal/noise ratio of the XAS spectrum. A Pd foil reference was scanned simultaneously for energy calibration. The Demeter software package was used for data processing and analysis. For calibration, normalization, and background subtraction, the Athena software was used. EXAFS modeling was performed using Artemis software. For generating scattering paths, the crystal structure of PdO was obtained from the Materials Project (mp-1336). To generate the Pd-Sn scattering paths, Pd atoms in the PdO structure were substituted with Sn atoms except the core atom. The amplitude reduction factor (S_0^2) of 0.78 ± 0.04 was obtained from modeling the EXAFS of PdO reference foil. The structures used are those shown in SI Figures S13-15, and were generated from the experimental structures of PdO [52] and SnO_2 [53]. The latter was cleaved along the (110) plane in order to expose the surface and place PdO_4 and Pd_2O_6 units extracted from the PdO.

FTIR spectroscopy was used to determine the sensing mechanism by probing CO interaction with the sensing layer, and to characterize the materials by studying their functional groups. ADC Pd/SnO_2, Pd NPs/SnO_2 and pure SnO_2 samples, weighing about 20 mg each, were first pressed into self-supporting pellets. These pellets were then loaded into a stainless-steel sample holder, which was subsequently placed in a custom-built in situ transmission IR cell. The cell was

designed with a cylindrical heater, and temperature was monitored using a K-type thermocouple (Omega) and controlled using an Omega CS8DPT controller. The spectra were collected using a Thermo Scientific Nicolet 6700 FTIR spectrometer equipped with a liquid-nitrogen-cooled MCT detector. In the FTIR measurements, the same exposure conditions were used as in the sensing measurements, allowing analysis of the surface species being formed in the course of gas exposure. Repeated FTIR spectra were recorded "in-situ" with 4 cm^{-1} resolution and collected in the 1300 – 4000 cm^{-1} region. Each spectrum was averaged over 120 scans, yielding time series of spectra separated by about 60 s. The sample was first annealed at 270 °C overnight under 100 $ml.min^{-1}$ of flowing air (Airgas, Ultra zero), and subsequently cooled to 60 °C for FTIR measurement (operating temperature in the sensor measurements). The sample film was first exposed to the dry air for 1 h to allow the system to equilibrate, then 1000 ppm of CO was admitted for 15 min, followed by purging in dry air at 300 sccm.

Sensor fabrication and test setup

Pt/Ti interdigitated electrodes (IDEs) with an active area of 3.5 mm in length, composed of 90 finger pairs of 5 µm width and spacing on a glass substrate (10 x 6 x 0.75 mm), were purchased from Micrux Technologies Ltd., Spain (Figure S2a and Figure S2b). The IDEs were sonicated in isopropyl alcohol, acetone, and deionized water (DI) for 15 min, respectively, and dried with nitrogen before use. The gas sensors were fabricated following three steps: a) drop-casting a colloidal solution of the as-synthesized catalysts (10 wt.% ink in ethanol) onto the pre-cleaned Pt-Ti interdigitated electrode; b) evaporation of the solvent at 50 °C; and c) post-deposition annealing treatment of the deposited sensing layer in ambient air at 275 °C for 3h to remove residual solvent and enhance its adherence and stability, and subsequent conductive wire-bonding (Figure S2c). Following the sensor fabrication, the contact between the sensing layer and the electrodes was examined *via* current-voltage (I-V) characteristic curves between 25-270 °C and confirmed to exhibit Ohmic characteristics.

Figure S3 shows the gas sensing test apparatus schematic and actual setup image. The fabricated interdigitated Pt/Ti electrode-based sensor was mounted on a circular ceramic miniature heater (Heat Scientific, OD05 X 1.2 mm) with a diameter of 5 mm. The test chamber is made from stainless steel and is around 13 cm^3 in volume. CO was selected as the target gas and dry air was used as the background atmosphere. The tested gas CO (Airgas, 0.1% in air) was diluted with pre-dried house air, and then flowed into the gas chamber with a total flow rate of 300 sccm controlled by mass flow controllers (MFC, Bronkhorst). The gas delivery system was controlled by a custom LabVIEW program. The sensor resistance was measured by a source-meter (Keithley 2602 A), which applies voltages through the sensor to monitor the sensor resistance. The temperature of the heater was controlled by an external DC power supply (Sorensen, DCS2600-1.7E) and measured by a thermocouple connected to the backside of the heater. Zephyr, an open-source Java-based software, was used to control the source-meter and acquire the real-time data from the source-meter and the gas delivery system. The resistance of the sensing layer was measured by the source-meter which applied a voltage through both sensor and heater channels to monitor the sensor resistance and to control heater temperature. The data from the source-meter was acquired by Zephyr. The gas response of the sensor was calculated as R_a/R_g, where R_a and R_g are the real-time steady state resistance values in air and after gas exposure, respectively. The response and recovery times are defined as the times for the sensor to achieve 90%

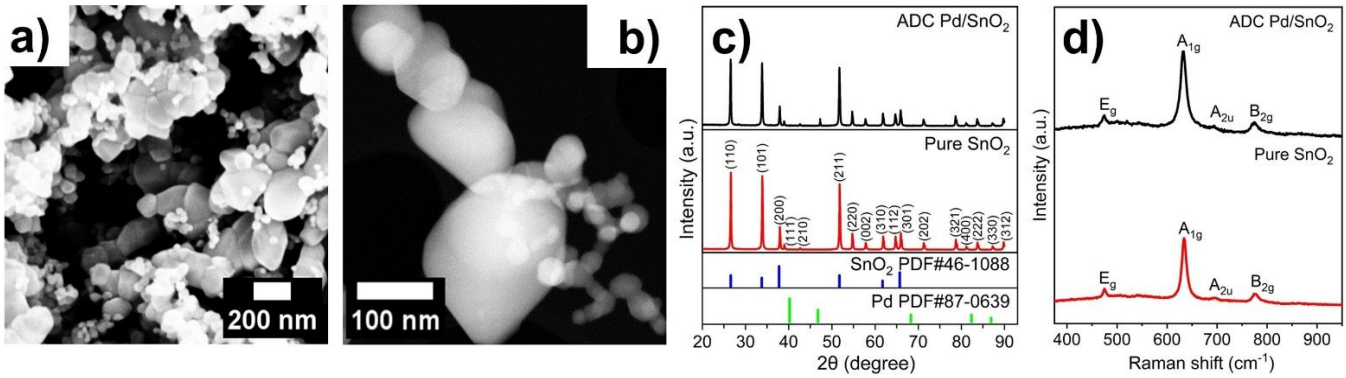

Figure 1. Structural and morphological characterizations of SnO_2 support and ADC Pd/SnO_2: a) FESEM image of SnO_2 support. Scale bar, 200 nm. b) STEM image of SnO_2 support. Scale bar, 50 nm. c) Powder XRD patterns of pure SnO_2 support annealed in ambient air at 500 °C with the reference data PDF card # 46-1088 (bottom, blue lines) and ADC Pd/SnO_2 with the reference data Pd PDF card # 87-0639 (bottom, green lines). d) Raman spectra of pure SnO_2 and ADC Pd/SnO_2.

of the final sensing or baseline signals, respectively, as shown in Figure S4.

Results and discussion

Materials characterization

FESEM and STEM images of the SnO_2 support demonstrate polycrystalline aggregates of polydisperse nanoparticles of 9-208 nm (Figures 1a and 1b and Figure S5a). FESEM images of Pd NPs/SnO_2 and ADC Pd/SnO_2 show similar morphology (Figures S6-S8). The powder X-ray diffraction (XRD) peaks of both SnO_2 support and ADC Pd/SnO_2 exhibit strong and sharp diffraction peaks characterizing tetragonal rutile phase of SnO_2, shown in Figure 1c. No Pd or PdO diffraction peaks or peaks associated with other impurity phases were observed in the ADC Pd/SnO_2. The Raman spectra of pure SnO_2 and ADC Pd/SnO_2 in Figure 1d show the Raman-active peaks and the IR-active mode of SnO_2, which corresponds to the rutile tetragonal structure of SnO_2, agreeing with the XRD pattern [54, 55], while no vibrational Raman modes of PdO are observed in the ADC Pd/SnO_2. N_2 adsorption-desorption isotherm of annealed SnO_2 suggests type II isotherm (Figure S5b), typical for non-porous materials, on which total Brunauer–Emmett–Teller (BET) surface area was calculated as 7.5 $m^2.g^{-1}$.

The energy dispersed X-ray spectra (EDS), and STEM-EDS elemental mapping illustrate that Pd, Sn and O elements are uniformly distributed in ADC Pd/SnO_2, given in Figure 2. High-resolution TEM image (Figure 2b) indicates an interplanar spacing of 0.35 nm corresponding to SnO_2 (110) which is the most thermodynamically stable and frequently observed surface of rutile SnO_2. These analyses are to be contrasted to Pd NPs/SnO_2 sample, where the EDS mapping and analysis, shown in Figures S7a and S7c confirm the presence of Pd nanoparticles. In particular, 10 nm Pd NP with lattice fringes of 0.215 nm, which corresponds to the *d* spacing of the (111) plane of Pd, are found in Pd NPs/SnO_2 (Figure S7b). However, high-angle annular dark field STEM images obtained on ADC Pd/SnO_2, presented in Figure 2d and Figure S8, are not able to identify single atoms or nanoparticles of Pd on these materials due to the similarity of Pd and Sn atomic numbers (46 vs. 50).

The Pd in ADC Pd/SnO_2 was quantified *via* ICP-OES, and the Pd loading was determined to be 0.73 ± 0.02 wt % (Figure S9). The measured loading, comparable to the nominal Pd loading (0.75 wt%), suggests that there is a sufficient number of surface sites on the SnO_2 for $Pd(OAc)_2$ adsorption at 25 °C. By combining this information with BET analysis, the Pd atom number density on SnO_2 was estimated to be:

$\rho_{Pd} = X_{Pd}N_A/M_{Pd}SSA_{SnO_2}$=5.6 at.nm^{-2},

where the wt% of Pd loading (X_{Pd}) is 0.73 ± 0.02 %, $N_A = 6.02\ E23$, the Pd molar mass $M_{Pd} = 106.42\ g.mol^{-1}$, and the specific surface area (SSA) of SnO_2 particles, from BET analysis, is 7.5 $m^2.g^{-1}$. This suggests that on average ~0.5 monolayer of Pd atoms covers SnO_2 support. X-ray photoelectron spectroscopy analyses (Figure S10) yield a similar value of 0.5 monolayer for Pd loading.

The surface electronic states and chemical compositions of ADC Pd/SnO_2 were investigated using X-ray photoelectron

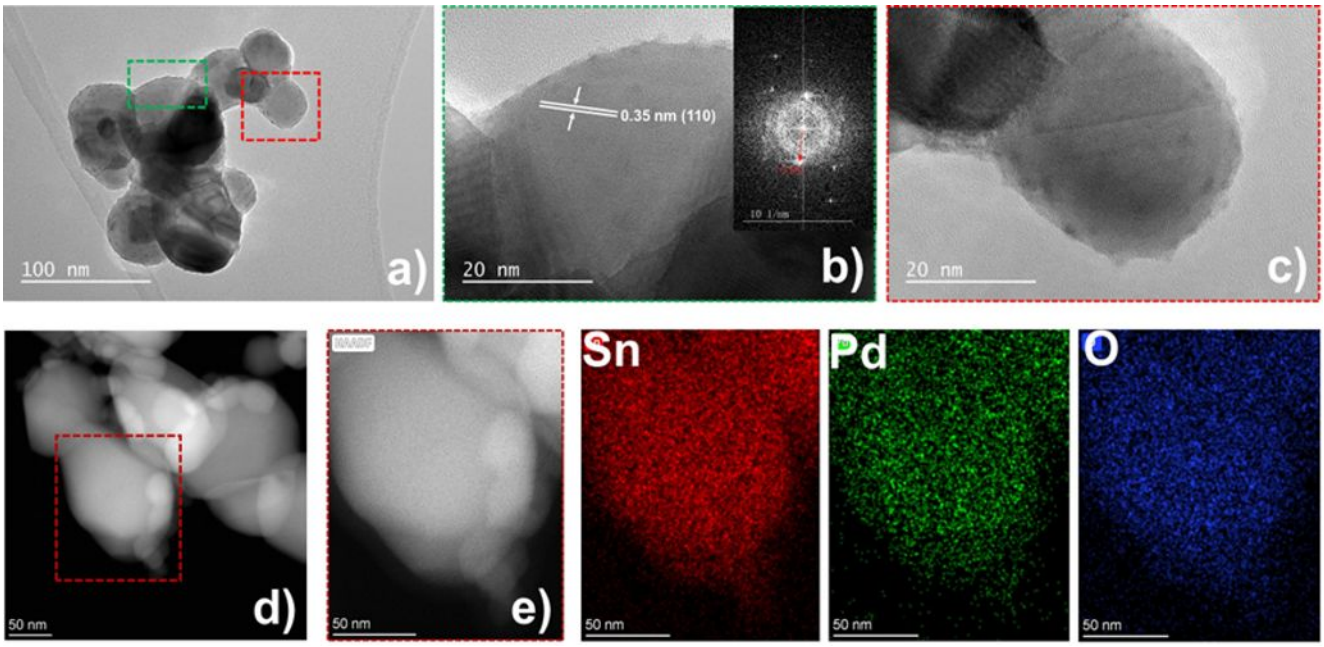

Figure 2. Structural and morphological characterization of ADC Pd/SnO_2: HRTEM images of ADC Pd /SnO_2 at a) low and b,c) high magnifications, respectively. Scale bars, 100 nm and 20 nm, respectively. d) HAADF-STEM images. Scale bar, 50nm. e) EDS elemental mapping. Scale bars, 50 nm.

spectroscopy (XPS) analyses, shown in Figure 3, where the presence of Pd, Sn and O is evidenced without any impurity elements, suggesting the formation of Pd-O-Sn based catalyst (Figure S10a). The high-resolution XPS spectra of Sn 3d and Pd 3d are shown in Figures 3a and 3b, respectively. XPS analyses of pure SnO_2 and ADC Pd/SnO_2 demonstrate that Sn $3d_{5/2}$ line is at the same position in the two samples, at 487.15 eV, which indicates that the electrical properties of the SnO_2 substrate/sample holder contact are identical in the two samples. The deconvoluted Pd 3d spectrum indicates that Pd is in two states, namely, metallic Pd^0 state being -presumably- small metallic clusters of Pd on the SnO_2 nanoparticles and PdO state being the single atoms, bonded to O atoms of the SnO_2 particles (schematically shown in Scheme Ic).

Figure 3c, were used to study the energy band structures of pure SnO_2 support and ADC Pd/SnO_2. The spectra show increased density of states at the Fermi level upon Pd incorporation in SnO_2, reflecting more metallic characteristics.

X-ray absorption spectroscopy (XAS) data at Pd K-edge were recorded on ADC Pd/SnO_2 and Pd NPs/SnO_2 to investigate the local electronic and geometric structure around the Pd atoms in the samples. The Pd K-edge X-ray absorption near edge structure (XANES) and the extended X-ray absorption fine structure (EXAFS) spectra of the samples are shown in Figure 4 (together with PdO as a reference). The Pd XAS of NP/SnO_2 sample shows resemblance to that of PdO in both XANES and EXAFS, in agreement with the ~20 nm-size PdO particles as revealed by TEM-EDS (Figure S7) and XPS

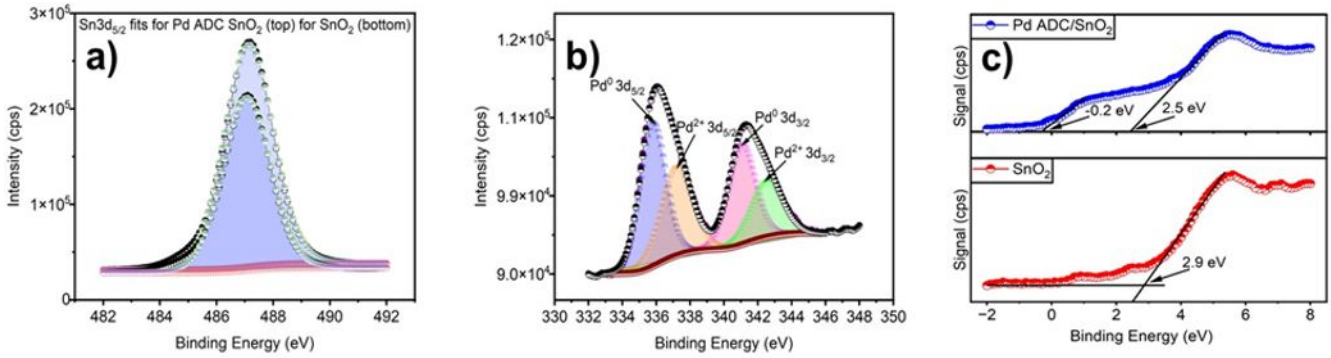

Figure 3. XPS characterization: a) Sn $3d_{5/2}$ region of ADC Pd/SnO_2 (top) and unloaded SnO_2 (bottom). b) Pd 3d region of ADC Pd/SnO_2. c) Valence band spectra of ADC Pd/SnO_2 (top) and unloaded SnO_2 (bottom).

XPS analyses were also conducted on Pd NPs/SnO_2 samples. The position of the Sn $3d_{5/2}$ line is also at 487.15 eV. This indicates that the electrical properties of the SnO_2 substrate/sample holder contact are identical in the three samples. In contrast to ADC Pd/SnO_2, however, only one component is present in the Pd region at 337.2 eV which indicates that the Pd line in the metallic Pd clusters is shifted by ~1.4 eV, consistent with the edge of the valence band density-of-states of the sample, or about half the band gap of SnO_2 (Figure S11c). Thus, the metallic clusters on the insulating surface of the Pd NPs/SnO_2 sample appear positively charged.

The valence band X-ray photoelectron spectra, shown in (Figure S11). The EXAFS of the Pd NPs/SnO_2 is adequately modelled using the coordination numbers and bond distances of bulk PdO, as shown in SI (Figure S13 and Table S3). However, the XAS of ADC Pd/SnO_2 shows differences in both XANES and EXAFS compared to spectra of both Pd NPs/SnO_2 and PdO. In the Pd K-edge XANES (Figure 4a), the white line feature at ~24367.0 eV is less pronounced for the ADC Pd/SnO_2 compared to that of Pd NPs/SnO_2 or bulk PdO, suggesting a different electronic structure of Pd atoms in the ADC sample. Indeed, a similar observation regarding the white line feature has been made by earlier works where the Pd is present as either single-site or small cluster [56-64].

Scheme I. Schematic illustration of synthesis of atomically dispersed tin (IV) oxide supported Pd catalyst: a) Wet deposition of $Pd(Oac)_2$. b) Proposed structure of the (-SnO_x)$Pd(OAc)_2$ surface complex, with the Pd center datively interacting with surface tin oxide. c) Thermal reduction of the resulting complex and proposed (-SnO_x)Pd surface complex structure, with the Pd center datively interacting with the surface tin oxide.

The EXAFS of ADC Pd/SnO_2 is drastically different from that of Pd NPs/SnO_2 or PdO. As shown in Figure 4b, the ADC Pd/SnO_2 EXAFS is missing high frequency *k*-space oscillations that are found in bulk structures, suggesting the lack of long-range order in the ADC structure which could indicate atomically dispersed Pd atoms and/or small-sized Pd clusters. The amplitude of the second shell peak positioned between 2.1-3.6 Å in the FT-EXAFS, shown in Figure 4c, is significantly reduced for the ADC sample compared to Pd NP and PdO. The Pd-Pd scattering from the next near Pd neighbor (at non-bonding distance of 3.0 Å) and the Pd-O-Pd scattering path at 3.4 Å contribute heavily to the second shell in PdO. The much weaker amplitude of the second shell feature observed for the ADC sample suggests the presence of either small PdO clusters or atomically dispersed Pd sites on SnO_2.

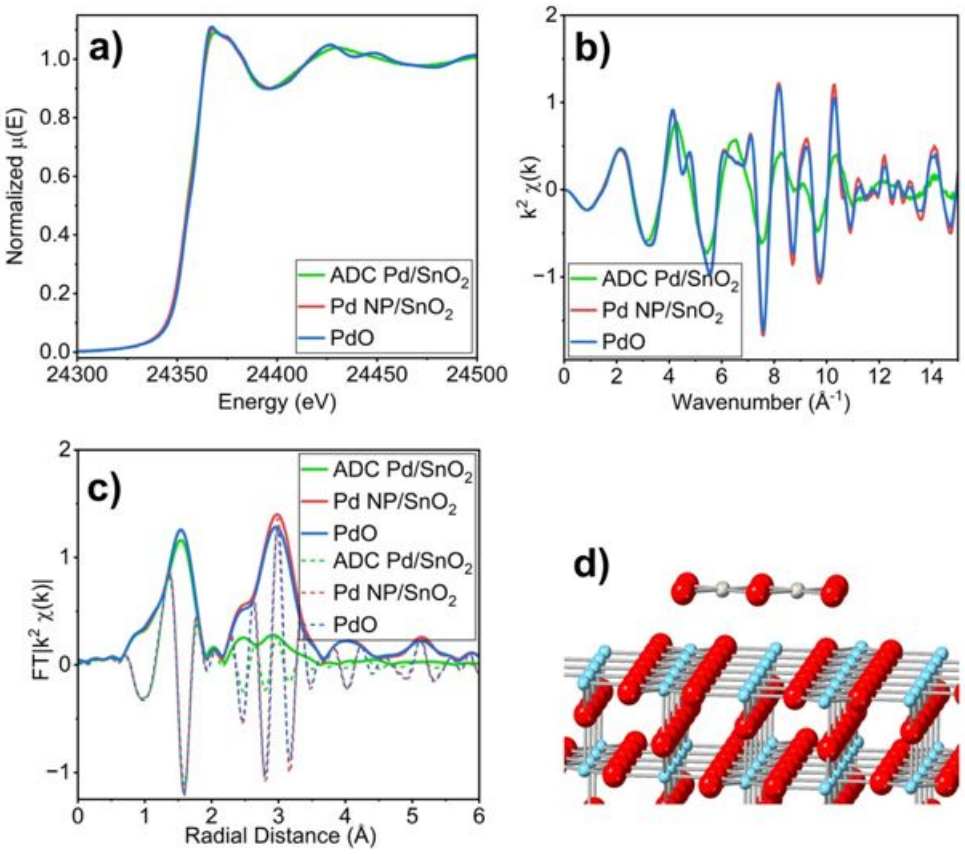

Figure 4. Pd K-edge XAS data for ADC Pd/SnO_2, Pd NPs/SnO_2, and the reference PdO. a) Normalized XANES spectra. b) k^2-weighted EXAFS spectra in *k*-space. c) k^2-weighted FT-EXAFS spectra in magnitude (solid) and imaginary (dotted) *R*-space. For Fourier transform, *k*-range of 3.0–13.5 $Å^{-1}$ was used. d) Proposed structure for ADC Pd/SnO_2 that is consistent with EXAFS analysis (Red: O, Grey: Pd, Blue: Sn).

To determine whether the Pd in the ADC sample is present as atomically dispersed or small clusters of PdO, EXAFS analysis has been performed to identify the scattering atom contributing to this second shell. If it is the atomically dispersed Pd atoms on SnO_2, the second shell contribution should be from the Pd-Sn scattering path. If it is small clusters of PdO, then the second shell will comprise the Pd-Pd scattering path. Unfortunately, Pd (Z=46) and Sn (Z=50) are too close in their atomic numbers to be confidently distinguished by XAS. The detailed comparison of the Pd-Pd and Pd-Sn scattering paths is presented in SI (Figure S14). This demonstrates the challenge in differentiating the Pd from Sn. The best fit EXAFS models of the ADC Pd/SnO_2 sample are also shown (Figure S15); Pd-Pd or Pd-Sn scattering paths equally produce an adequate fit. However, despite the challenge in identifying of the scatterer, the EXAFS results still provide insight into the structure of the ADC Pd/SnO_2. The small CN values of 1 or less for the paths contributing to the second shell suggest high dispersion of Pd. To gain more in-depth understanding of the structure, several catalyst structures were proposed based on the CN values determined from the EXAFS modeling. The small CN values of 1 or less for the Pd-Pd/Sn paths at distances ~3.0 Å and ~3.4 Å are satisfied by the structure in which PdO_4 or Pd_2O_6 units lie flat on the surface of SnO_2 (Figure 4d). Other structures that have these types of units anchored vertically on the SnO_2 surface do not give the scattering distances that agree with the EXAFS fitting results,

as shown in the SI (Figure S16 and Table S5). The XAS data strongly suggest that the ADC sample is likely to be highly dispersed, low-dimensional Pd clusters on the SnO_2 surface.

Gas sensing results

Gas sensing performance of ADC Pd/SnO_2 was evaluated in a setup as described earlier in the experimental section. All gas exposure tests were performed a dry condition. The ADC Pd/SnO_2 material was operated in a temperature range of 25-270 °C. Figure 5 shows the dynamic response-recovery curve of ADC Pd/SnO_2 sensor to 100 ppm CO exposure at 60 °C. For each dynamic measurement cycle, the sensor resistance is allowed to reach a stable baseline resistance at constant flow of dry air, and subsequently the sensor is exposed to CO. Upon exposure, the resistance of ADC Pd/SnO_2 rapidly and significantly decreases which indicates *n*-type characteristics of ADC Pd/SnO_2. The sensor resistance recovers to the initial baseline resistance when purged with dry air, indicating its good reversibility, repeatability, and stability over multiple exposure cycles. Figure 5b displays a zoomed-in dynamic response / recovery curve of the sensor during a 100 ppm exposure and removal cycle. The sensor response R_a/R_g is 140 ± 15, with a response time of 11.4 ± 0.9 s and a recovery time of 30.4 ± 5.0 min. The slower recovery to the baseline after gas exposure is attributed to slow desorption rate at low working temperature, and to the surface morphology and non-porosity of the polycrystalline aggregates of SnO_2 nanoparticle support. The recovery time can be accelerated by integrating an auxiliary local microheater, only activated after gas exposure without affecting the sensing mechanism of the sensor [15].

The response of the ADC Pd/SnO_2 sensor at 60 °C to various CO concentrations was also examined. Figure 6a displays the dynamic response-recovery curves to 5-100 ppm CO concentration range while Figure 6b shows these curves for lower concentration range of 0.25 – 5 ppm. The amount of change in the sensor resistance increases with increasing concentration due to the increased surface reactions between adsorbed CO and oxygen species. The sensor response data

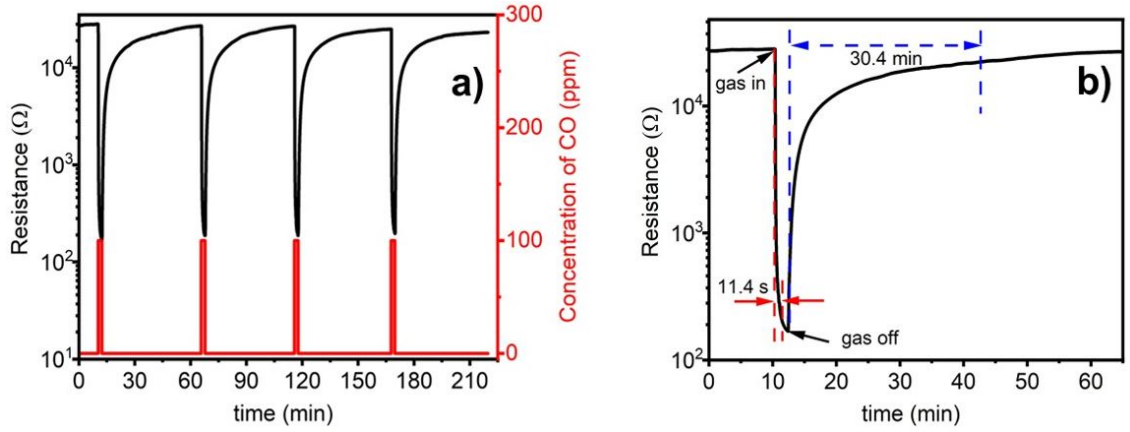

Figure 5. Dynamic response and recovery curves of the ADC Pd/SnO_2 sensor upon exposure to 100 ppm CO at 60 °C: a) Sensor resistance response (black) to CO pulses (red) in a semi-log plot. b) Dynamic response / recovery curve of the sensor during the first gas exposure and removal cycle, indicating the sensor response and response/recovery times.

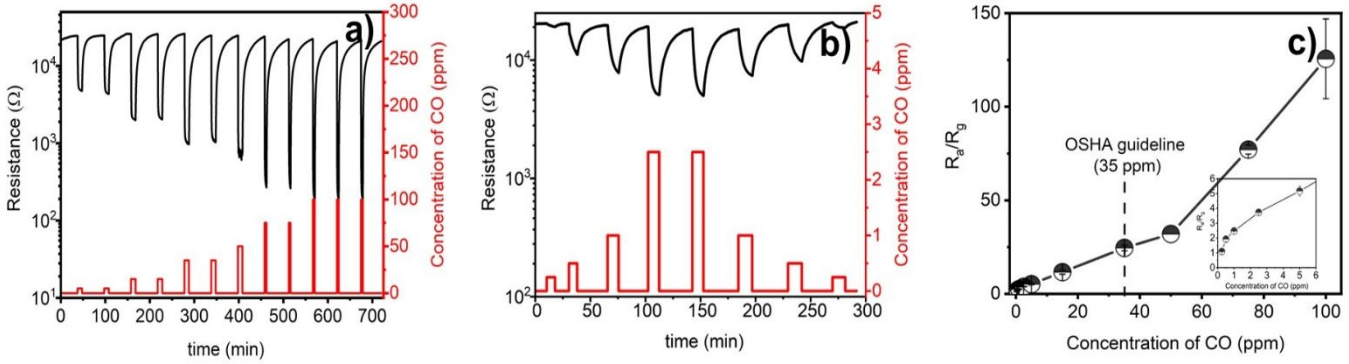

Figure 6. Dynamic response and recovery curves of the sensor upon exposure to 0.25-100 ppm CO at 60 °C: a) Sensor resistance concentration log–log plot of ADC Pd/SnO_2 to 5-100 ppm CO. b) Sensor resistance concentration log plot of ADC Pd/SnO_2 to 5-100 ppm CO. c) Sensor response to CO at varying concentrations between 0.25-100 ppm at 60 °C. The inset in Figure 6c illustrates the sensor response to CO for concentration range of 0.25 – 5 ppm.

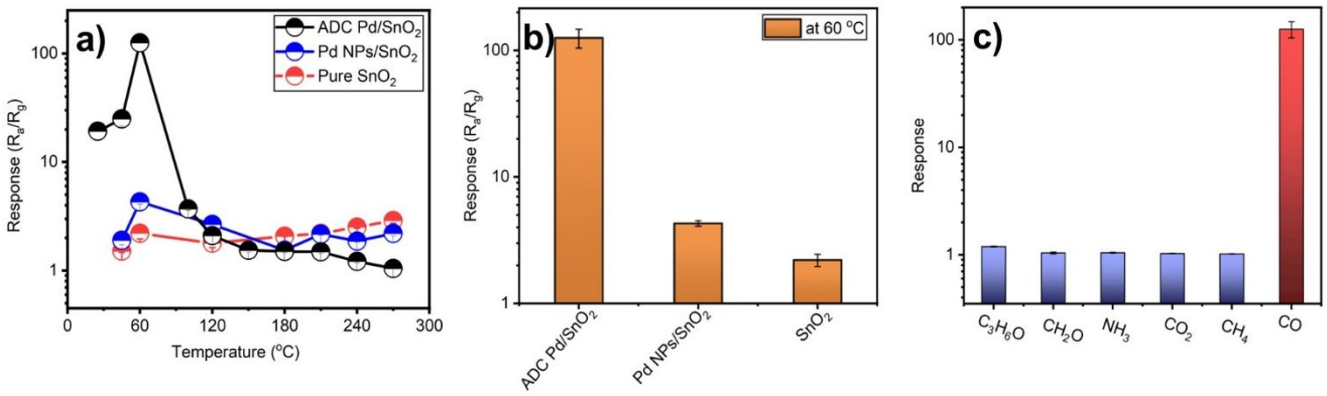

Figure 7. a) ADC Pd/SnO_2 sensor response to 100 ppm CO vs. operating temperatures and its comparison with pure SnO_2 and Pd NPs/SnO_2 gas sensors. b) Column charts of responses to 100 ppm CO of ADC Pd/SnO_2, Pd NPs/SnO_2 and pure SnO_2 sensors. c) Responses of ADC Pd/SnO_2 operated at 60 °C to different interferant gases (400 ppm acetone, 2.5 ppm formaldehyde, 50 ppm ammonia, 5000 ppm carbon dioxide, 5000 ppm methane and 100 ppm carbon monoxide).

are summarized in Figure 6c, with the inset showing the data for concentration range of 0.25 – 5 ppm. The noise level and theoretical LOD of the sensor was calculated using the root-mean-square (RMS) error at the baseline and the slope of the response curve (Equation S3). The linear fitting of the plot between 1-35 ppm deduces limit of detection (LOD), 3 times the noise standard deviation, as 0.37 ppm (Figure S17).

Furthermore, the sensor was tested against 100 ppm CO exposure at various operating temperatures in the range of 25 – 270 °C. Figure 7a demonstrates temperature-dependent response, on a semilog plot, of ADC Pd/SnO_2 to 100 ppm CO. Unlike typical SnO_2-based sensors, ADC Pd/SnO_2 show high response at low temperatures. The response gradually increases and reaches a maximum at 60 °C, beyond which the response decreases. For comparison, Figures 7a and 7b also display the response values of sensors based on Pd NPs/SnO_2 and pure SnO_2 (raw data in SI, S19 and S20). The results show that the ADC Pd/SnO_2 outperforms both, exhibiting much higher sensitivity to CO (a factor of 30 with respect to Pd NPs/SnO_2), highlighting the enhanced catalytic activity of ADC Pd. This is attributed to the exceptional ability of ADC Pd to generate sites that are more reactive and reduces the activation energy for adsorption of CO [65-67]. Furthermore, atomic Pd provides a higher adsorption efficiency for oxygen species, and hence enhances the sensitivity and selectivity toward CO.

ADCs are also expected to exhibit improved selectivity. As shown in Figure 7c, ADC Pd/SnO_2 exhibits superior response to CO and two orders of magnitude lower response toward 5 different interference analytes at various concentrations (400 ppm acetone, 2.5 ppm formaldehyde, 50 ppm ammonia, 5000 ppm carbon dioxide, 5000 ppm methane and 100 ppm CO).

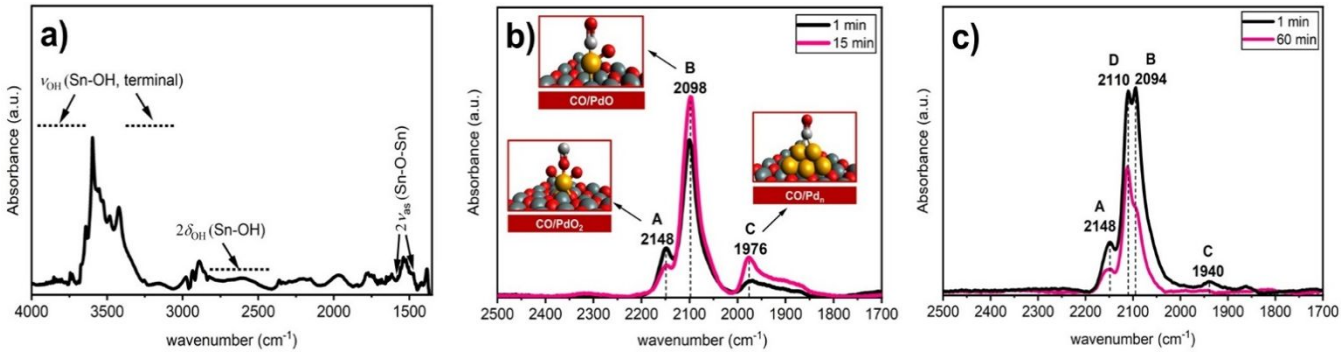

Figure 8. *In situ* IR spectra of CO adsorption and desorption for ADC Pd/SnO_2 in air at 60 °C and at ambient pressure: a) Prior to CO exposure after calcination at 270 °C (4000-1300 cm^{-1}region); b) During the dosing of 1000 ppm CO at 1 min and 15 min (2500–1700 cm^{-1} region). Inset figures show illustration of the different CO adsorption sites on ADC Pd/SnO_2. Pd, Sn, C, and O atoms are displayed as orange, dark gray, light gray and red spheres, respectively (Figure S22): CO linearly adsorbed on isolated, positively charged single Pd atoms, CO linearly adsorbed on atop geometry on Pd single atoms bound to SnO_2 support *via* one oxygen atom; bridged adsorption of CO on metallic Pd clusters; c) During CO removal by air purge, acquired at 1 min and 60 min (2500–1700 cm^{-1} region).

The concentrations are chosen because some toxic effects occur beyond these values over long-term exposures [7, 68, 69].

In-situ FTIR measurements

In-situ FTIR measurements were performed to provide further insight into the dispersion and oxidation state of Pd, and to characterize surface adsorption of CO on ADC Pd/SnO_2 (and for comparison on SnO_2 and Pd NP/SnO_2), examining their interfacial and host-guest interactions, thereby to unravel the sensing mechanism.

spectrum, which suggests that it is completely removed from the Pd site during the above-mentioned annealing step (Figure S1). The CO IR spectra of ADC Pd/SnO_2 reveals three sets of CO absorption bands centered at 2148 (A), 2098 (B) and 1976 cm^{-1} (C) [92-95]. Adsorbed CO was not present on the bare SnO_2 sample under our experimental conditions (Figure S21), which indicates that these bands originate from CO molecules adsorbed on three Pd species. The band around 2148 cm^{-1} (A) is assigned to a-top CO on single isolated Pd^{2+}

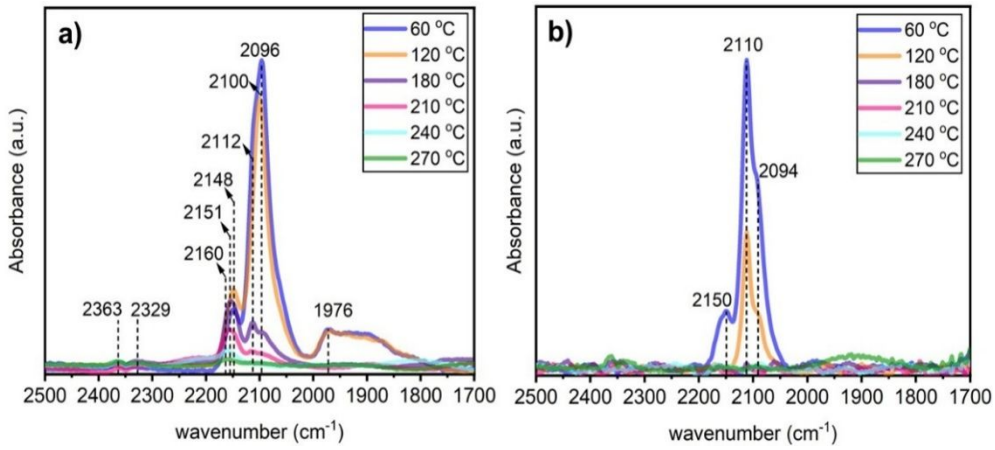

Figure 9. *In situ* IR spectroscopy of CO interaction with ADC Pd/SnO_2 at various temperatures in the range between 60-270 °C: a) In presence of CO; b) Air purge.

Figure 8 shows IR spectra of ADC Pd/SnO_2 held at 60 ˚C, recorded in dry air flow (Figure 8a), followed by 15 min dosing of 1000 ppm CO in air (Figure 8b), and during desorption in air flow for 1h (Figure 8c). The dry air flow over the sample yields several bands: a peak around 3500 cm^{-1}, and a broad band centered around 3000 cm^{-1} [ν_{OH} (Sn-OH)], a broad band centered around 2400 cm^{-1} [$2\delta_{OH}$ (Sn-OH)] and two bands around 1500 cm^{-1} and 1400 cm^{-1} [$2\nu_{as}$ (Sn-OH)] (Figure 8a) [92]. Furthermore, no spectral markers of acetate are found in the sites (Pd_1O_2) [70-72], the IR peak at 2098 cm^{-1} (B) is ascribed to CO molecules linearly adsorbed in an a-top geometry on Pd single atoms bound to SnO_2 *via* one oxygen atom (Pd_1O_1) [70-74], and the band around 1976 cm^{-1} (C) is assigned to bridged adsorption of CO on two Pd atoms [70-80]. The formation of bridge-bonded CO indicates the existence of dimer or small metallic Pd clusters [71, 72, 80], which is in good agreement with EXAFS and XPS, and consistent with Scheme I. The weak broad band visible around 2300 cm^{-1} corresponds to CO_2 evolution.

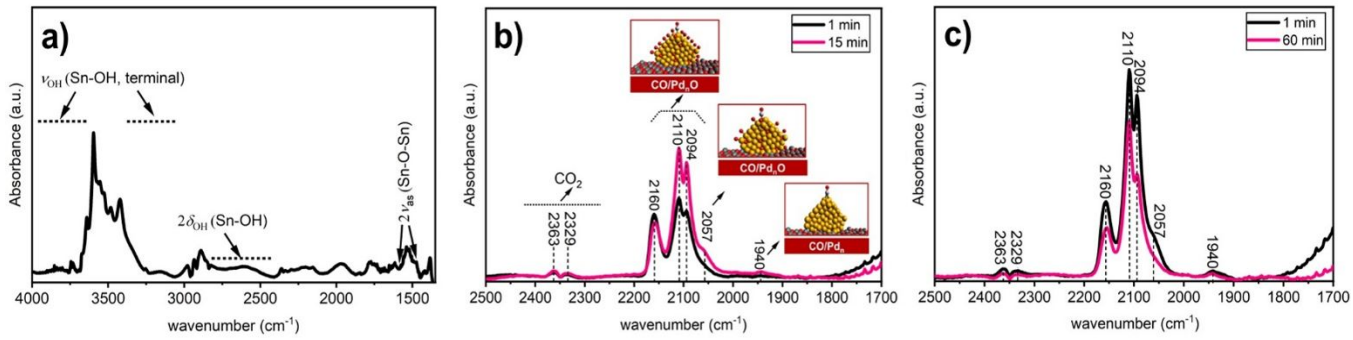

Figure 10. *In situ* IR spectroscopy of CO interaction with Pd NPs/SnO_2 in air at 60 °C and at ambient pressure after calcination at 270 °C: a) Prior to CO exposure (4000-1300 cm^{-1}), after *in situ* annealing in air; b) During dosing of 1000 ppm CO collected at various times (2500–1700 cm^{-1}). Inset figures show illustration of the different CO adsorption sites on Pd NPs/SnO_2. Pd, Sn, C, and O atoms are displayed as orange, dark gray, light gray and red spheres, respectively (Figure S24): CO linearly adsorbed on atop oxidized and semi-oxidized Pd NPs or nanoclusters; and bridging CO adsorbed on metallic Pd NPs. c) 1 min (black) and 60 mins (pink) after air purge step (2500-1700 cm^{-1}).

This indicates that these palladium carbonyl bands are associated with the sites that are active for the low temperature CO oxidation in gas sensing mechanism.

During desorption, the band around 1976 cm^{-1} first slightly shifted to 1940 cm^{-1} and disappeared over time, while a new band at ~ 2110 cm^{-1} (D) evolved gradually, and the band B shifted to 2094 cm^{-1} [78, 94, 95]. This suggests that Pd^0 gradually oxidized by oxygen in the air [81].

Additionally, FTIR spectra acquired at various temperatures between 120 and 270 °C (Figure S23) reveal that low-temperature exposure to CO at 60 °C and 120 °C facilitates its adsorption on Pd^{2+} and Pd^0 sites (Figure 9a), while at high temperatures, the intensity of these bands significantly decreases, which suggests that CO readily resides on Pd sites and finds better interaction at low temperatures, and quickly desorbs from the Pd surface at higher temperatures (Figure 9b). This confirms the reported sensing results which show enhanced performance of ADC Pd/SnO_2 at low temperatures.

In comparison, the IR spectra on Pd NPs/SnO_2, acquired in dry air flow at 60 °C after *in situ* calcination exhibit the same bands as the ADC Pd/SnO_2 (Figure 10a). However, the spectra upon exposure to CO (Figure 10b) are different: pronounced bands at 2160, 2110, 2094 cm^{-1} with a shoulder around 2057 cm^{-1}, appeared with increasing intensity upon CO exposure. These bands can be ascribed to CO linearly bonded to oxidized and semi-oxidized Pd NPs on edges, steps, and terraces of (100) and (111) facets, and might be associated with the active sites for low temperature CO oxidation in air [72, 82, 83]. The bands centered at 2329, and 2363 cm^{-1} prove the transient formation of gas-phase CO_2 during exposure to CO in air [72, 84]. The weak broad band centered around 1940 cm^{-1}, is ascribed to linear and bridge-bonded CO on metallic Pd nanoparticles (Figure 10b). This may imply reduction of PdO particles in the presence of CO [85]. These IR bands gradually increased in intensity with exposure time and decreased during the desorption process; yet did not disappear with the air purge (Figure 10c).

Proposed Gas Sensing Mechanism

The *In-situ* FTIR studies, coupled to the detailed characterization of ADC Pd/SnO_2 and prior studies on the catalytic activities of atomically dispersed noble metals on metal oxides [71, 72, 86, 87], allows us to put forth the following mechanism for CO sensing. The working mechanism of a chemiresistive metal oxide gas sensor is associated with gas-solid interactions between the sensor surface, target gas and adsorbed oxygen, involving gas diffusion, adsorption, spillover, surface reactions and gas desorption. When gas comes into direct contact with the sensor, a chemical reaction occurs that results in a change in the electrical resistance of the sensing layer. This change might take place due to the presence of target gas and/or ambient oxygen molecules. Oxygen adsorption initiates gas-sensitive response in metal oxides [88-90]. Active oxygen species are involved in the surface reactions as reactants, whose concentrations on the surface of the sensing material substantially affect the sensitivity [12]. Under atmospheric conditions, oxygen vacancies act as adsorption sites for molecular and atomic oxygen species. Adsorbed molecular oxygen may dissociate into two atomic oxygen species over Pd and spill over onto SnO_2 (Scheme IIa), forming molecular (O_2^-) and/or atomic (O^-, O^{2-}) species that capture electrons from the conduction band (R.1-R3) [91]. This creates a space charge layer (depletion layer), and

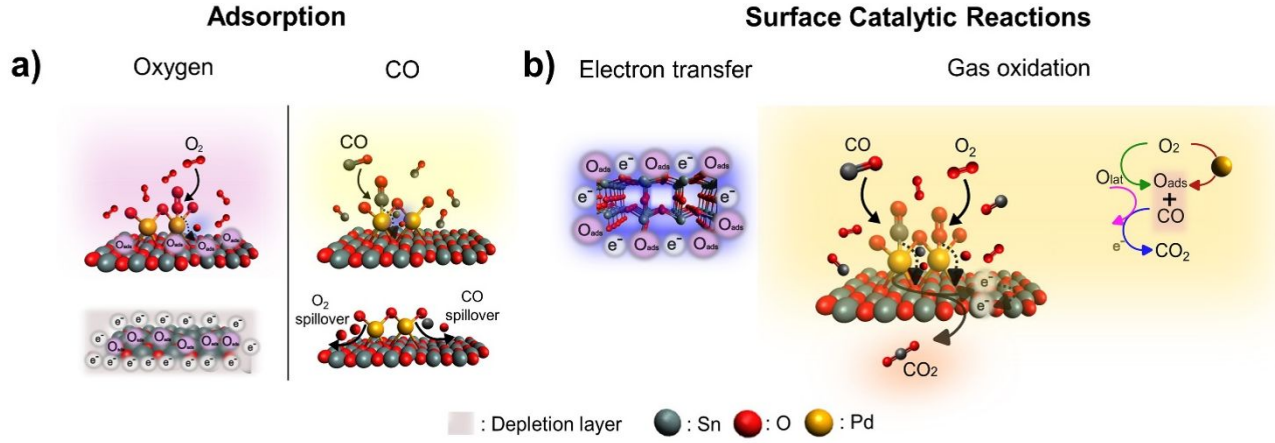

Scheme II. Schematic illustration of the proposed synergistic sensitization effects of the ADC Pd/SnO_2 sensor toward CO. O_{ads}: the surface adsorbed oxygen. a) CO/O_2 adsorption on the ADC Pd/SnO_2. b) Surface catalytic reactions on the Pd sites.

$$O_{2gas} \leftrightarrow O_{2ads} \quad \text{(R.1)}$$

$$O_{2ads} + V_O + e^- \leftrightarrow O^-_{2ads} \quad \text{(R.2)}$$

$$O^-_{2ads} + V_O + e^- \leftrightarrow 2O^-_{ads} \quad \text{(R.3)}$$

consequently a barrier to the charge carrier flow at the grain boundaries, resulting in increased resistance (Scheme IIa).

The active oxygen species formed on the ADC Pd/SnO_2 surface can be determined by the relationship between the sensor response and the CO concentration [92, 93]. According to these gas adsorption models, the relationship between the CO concentration, *C*g, and the sensor response, S_g (defined previously as R_a/R_g), can be expressed by Equation 1:

$$S_g = 1 + A_g C_g^{\beta} \quad (1)$$

where A is the prefactor and *β* is the surface species charge parameter having a value of 1 for O^- and 0.5 for O^{2-} [92, 93]. By fitting the experimental data to Equation 1 (Figure S26), the *β* value of the ADC Pd/SnO_2 is found to be close to 1, indicating that the adsorbed oxygen on the ADC Pd/SnO_2 is mainly O^-.

Activation of CO on Pd may involve its dissociation or a weakening of intramolecular bonds by the adsorption on the Pd sites, e.g. by the partial filling of anti-bonding molecular orbitals. Consistent with the proposed mechanism for CO oxidation over ADC Pd on various metal oxides such as CeO_2 and TiO_2 [13, 94, 95], *in-situ* FTIR measurements in CO-air (Figure 8 and 9) reveal that Pd provides favorable adsorption and activation sites for CO (bands (A), (B) and (C) in Figure 8b), from which activated fragments are spilled over onto the SnO_2, forming CO_2 by the reactions of adsorbed CO with the 2-fold bridging oxygen forming an oxygen vacancy (R4), and with the active oxygen species (O^-) (R5) (Scheme IIa). This results in the release of electrons back to the conduction band and locally decreasing depletion layer and consequently a decrease in the resistance [72, 82, 83]. The band around 2300 cm^{-1} in Figure 8b proves the transient formation of gas-phase CO_2 during exposure to CO [72, 84] (Scheme IIb).

$$CO + O_O^{2-} \leftrightarrow CO_{2,gas} + V_O^{++} + 2e^- \quad (R.4)$$

$$CO + O^- \rightarrow CO_{2,gas} + e^- \quad (R.5)$$

Lastly, in agreement with various infrared spectroscopic studies [91, 96, 97], the weak bands in the 1850-1300 cm^{-1} region in Figure S21 suggest formation of various surface carbonate and related species (~1600-1300 cm^{-1}), upon CO adsorption and its reaction with active oxygen on the surface of SnO_2, which are consequently decomposed into CO_2 (~ 1700 cm^{-1}) [98]. Specifically, the bands ~ 1400-1350 cm^{-1} implies the formation of monodentate carbonate (CO_3^-), as O_2^- most likely reacts with CO (R.6 and R.7) [84].

$$CO + O_2^- \rightarrow CO_3^- \rightarrow CO_2 + O^- \quad (R.6)$$

$$CO_2 + O^- \leftrightarrow CO_3^- \quad (R.7)$$

Conclusions

SnO_2-supported Pd single atoms coupling with small cluster structures were developed via a simple method. Benefiting from the synergistic effect, coupling the advantages of Pd single atoms and small clusters on catalysis, exceptional performance and selectivity toward CO among commonly existing interference gases were acquired at low temperatures in comparison to pure SnO_2 and Pd NPs/SnO_2. The results of detailed characterizations confirm that the unique chemical and electronic structure of ADC Pd/SnO_2 possesses moderate adsorption strength for CO and promotes the adsorption and dissociation of oxygen and CO, creating abundant active interfacial oxygen species, which synergistically facilitate catalysis, decreasing the energy barrier and significantly improving the sensitivity. This work may open a robust and versatile avenue for the realization of a variety of ADCs in chemical sensing, and for the fabrication of a new generation of sensing materials with enhanced performance and sensor devices.

Author contributions

Yaprak Ozbakir: Conceptualization, Methodology, Investigation, Validation, Visualization, Writing – original draft. Yong Xia: Writing – review & editing. Aifei Pan: Writing – review & editing. Jiyun Hong: Investigation, Writing – review & editing, Visualization. Jorge E. Perez-Aguilar: Investigation. Simon Bare: Writing – review & editing. Francesca Rossi: Investigation. Rohan Dhall: Investigation. Afnan Ali Alghannam: Investigation. Nishit Goel: Writing – review & editing, Resources. Stephen Bart: Writing – review & editing, Resources. Carlo Carraro: Conceptualization, Investigation, Writing – review & editing, Supervision, Project administration. Roya Maboudian: Conceptualization, Writing – review & editing, Supervision, Resources, Project administration, Funding acquisition.

Conflicts of interest

The authors declare that they have no known competing financial interests or personal relationships that could have appeared to influence the work reported in this paper.

Data availability

Data will be made available on request.

Acknowledgements

This study was primarily supported by the U.S. National Science Foundation under grant no 2224465, the industrial members of the Berkeley Sensor & Actuator, and the Scientific and Technological Research Council of Turkey (TUBITAK) 2219-International Postdoctoral Research Fellowship Program (App. No: 1059B192000201). The authors thank Prof. Fernando D. Vila for valuable discussions regarding the XAS data and analyses. Co-ACCESS, part of the SUNCAT Center for Interface Science and Catalysis, is supported by the U.S. Department of Energy, Office of Basic Energy Sciences, Chemical Sciences, Geosciences and Biosciences Division. Work at the Molecular Foundry was supported by the Office of Science, Office of Basic Energy Sciences, of the U. S. Department of Energy under contract no DE-AC02-05CH11231. The authors thank Dr. Virginia Altoe for her assistance with TEM characterization. Y. X. would also like to acknowledge National Natural Science Foundation of China (No.52305615).

Notes and references

1. M. Mannan and S. G. Al-Ghamdi, *Int J Environ Res Public Health*, 2021, **18**.
2. J. Lee, Y. Jung, S.-H. Sung, G. Lee, J. Kim, J. Seong, Y.-S. Shim, S. C. Jun and S. Jeon, *Journal of Materials Chemistry A*, 2021, **9**, 1159-1167.
3. P. Kumar, A. B. Singh, T. Arora, S. Singh and R. Singh, *Science of The Total Environment*, 2023, **872**, 162163.
4. S. S. Shetty, D. D, H. S, S. Sonkusare, P. B. Naik, N. S. Kumari and H. Madhyastha, *Heliyon*, 2023, **9**, e19496.
5. S. Y. Kim, S. H. Kim, J. H. Wee, C. Min, S.-M. Han, S. Kim and H. G. Choi, *Scientific Reports*, 2021, **11**, 5108.
6. A. Lewis and P. Edwards, *Nature*, 2016, **535**, 29-31.
7. G. Jung, S. Hong, Y. Jeong, W. Shin, J. Park, D. Kim and J.-H. Lee, *ACS Applied Materials & Interfaces*, 2022, **14**, 17950-17958.
8. S. M. Majhi, A. Mirzaei, H. W. Kim, S. S. Kim and T. W. Kim, *Nano Energy*, 2021, **79**, 105369.
9. R. J. Rath, S. Farajikhah, F. Oveissi, F. Dehghani and S. Naficy, *Advanced Engineering Materials*, 2023, **25**, 2200830.
10. E. Ciftyurek, Z. Li and K. Schierbaum, *Sensors*, 2023, **23**, 29.
11. H. Ji, W. Zeng and Y. Li, *Nanoscale*, 2019, **11**, 22664-22684.
12. J. Zhang, X. Liu, G. Neri and N. Pinna, *Advanced Materials*, 2016, **28**, 795-831.
13. X.-L. Ye, S.-J. Lin, J.-W. Zhang, H.-J. Jiang, L.-A. Cao, Y.-Y. Wen, M.-S. Yao, W.-H. Li, G.-E. Wang and G. Xu, *ACS Sensors*, 2021, **6**, 1103-1110.
14. D. Degler, U. Weimar and N. Barsan, *ACS sensors*, 2019, **4**, 2228-2249.
15. Y. Ren, W. Xie, Y. Li, J. Ma, J. Li, Y. Liu, Y. Zou and Y. Deng, *ACS Central Science*, 2021, **7**, 1885-1897.
16. B. C. Gates, A. Katz and J. Liu, *Precis Chem*, 2023, **1**, 3-13.
17. Y. Lin, Y. Cao, Q. Yao, O. J. H. Chai and J. Xie, *Industrial & Engineering Chemistry Research*, 2020, **59**, 20561-20581.
18. L. Liu and A. Corma, *Chemical Reviews*, 2018, **118**, 4981-5079.
19. B. C. Gates, *Trends in Chemistry*, 2019, **1**, 99-110.
20. S. K. Kaiser, Z. Chen, D. Faust Akl, S. Mitchell and J. Pérez-Ramírez, *Chemical Reviews*, 2020, **120**, 11703-11809.
21. S. Mitchell and J. Pérez-Ramírez, *Nature Communications*, 2020, **11**, 4302.
22. J. Resasco, L. DeRita, S. Dai, J. P. Chada, M. Xu, X. Yan, J. Finzel, S. Hanukovich, A. S. Hoffman, G. W. Graham, S. R. Bare, X. Pan and P. Christopher, *Journal of the American Chemical Society*, 2020, **142**, 169-184.
23. L. Wang, H. Liu, J. Zhuang and D. Wang, *Small Science*, 2022, **2**, 2200036.
24. Y. Wang, X. Cui, J. Zhang, J. Qiao, H. Huang, J. Shi and G. Wang, *Progress in Materials Science*, 2022, **128**, 100964.
25. J. Park, S. Lee, H.-E. Kim, A. Cho, S. Kim, Y. Ye, J. W. Han, H. Lee, J. H. Jang and J. Lee, *Angewandte Chemie International Edition*, 2019, **58**, 16038-16042.
26. R. Zhang, Y. Li, X. Zhou, A. Yu, Q. Huang, T. Xu, L. Zhu, P. Peng, S. Song, L. Echegoyen and F.-F. Li, *Nature Communications*, 2023, **14**, 2460.
27. J. Li, M. Chen, D. A. Cullen, S. Hwang, M. Wang, B. Li, K. Liu, S. Karakalos, M. Lucero, H. Zhang, C. Lei, H. Xu, G. E. Sterbinsky, Z. Feng, D. Su, K. L. More, G. Wang, Z. Wang and G. Wu, *Nature Catalysis*, 2018, **1**, 935-945.
28. J. Zhang, H. Yang and B. Liu, *Advanced Energy Materials*, 2021, **11**, 2002473.
29. J. Chang, M. J. Hülsey, S. Wang, M. Li, X. Ma and N. Yan, *Angewandte Chemie*, 2023, **135**, e202218265.
30. J. Lin, A. Wang, B. Qiao, X. Liu, X. Yang, X. Wang, J. Liang, J. Li, J. Liu and T. Zhang, *Journal of the American Chemical Society*, 2013, **135**, 15314-15317.
31. J. Liu, *ACS Catalysis*, 2017, **7**, 34-59.
32. J.-C. Liu, Y.-G. Wang and J. Li, *Journal of the American Chemical Society*, 2017, **139**, 6190-6199.
33. S. Weon, D. Huang, K. Rigby, C. Chu, X. Wu and J.-H. Kim, *ACS ES&T Engineering*, 2021, **1**, 157-172.
34. M. Babucci, A. Guntida and B. C. Gates, *Chemical Reviews*, 2020, **120**, 11956-11985.
35. Z. Li, Y. Chen, S. Ji, Y. Tang, W. Chen, A. Li, J. Zhao, Y. Xiong, Y. Wu, Y. Gong, T. Yao, W. Liu, L. Zheng, J. Dong, Y. Wang, Z. Zhuang, W. Xing, C.-T. He, C. Peng, W.-C. Cheong, Q. Li, M. Zhang, Z. Chen, N. Fu, X. Gao, W. Zhu, J. Wan, J. Zhang, L. Gu, S. Wei, P. Hu, J. Luo, J. Li, C. Chen, Q. Peng, X. Duan, Y. Huang, X.-M. Chen, D. Wang and Y. Li, *Nature Chemistry*, 2020, **12**, 764-772.
36. S. Wei, A. Li, J.-C. Liu, Z. Li, W. Chen, Y. Gong, Q. Zhang, W.-C. Cheong, Y. Wang, L. Zheng, H. Xiao, C. Chen, D. Wang, Q. Peng, L. Gu, X. Han, J. Li and Y. Li, *Nature Nanotechnology*, 2018, **13**, 856-861.
37. Y. Chen, S. Ji, W. Sun, W. Chen, J. Dong, J. Wen, J. Zhang, Z. Li, L. Zheng, C. Chen, Q. Peng, D. Wang and Y. Li, *Journal of the American Chemical Society*, 2018, **140**, 7407-7410.
38. C. H. Choi, M. Kim, H. C. Kwon, S. J. Cho, S. Yun, H.-T. Kim, K. J. J. Mayrhofer, H. Kim and M. Choi, *Nature Communications*, 2016, **7**, 10922.
39. H. B. Yang, S.-F. Hung, S. Liu, K. Yuan, S. Miao, L. Zhang, X. Huang, H.-Y. Wang, W. Cai, R. Chen, J. Gao, X. Yang, W. Chen, Y. Huang, H. M. Chen, C. M. Li, T. Zhang and B. Liu, *Nature Energy*, 2018, **3**, 140-147.

40. G. Lei, H. Pan, H. Mei, X. Liu, G. Lu, C. Lou, Z. Li and J. Zhang, *Chemical Society Reviews*, 2022, **51**, 7260-7280.
41. H. Shin, W.-G. Jung, D.-H. Kim, J.-S. Jang, Y. H. Kim, W.-T. Koo, J. Bae, C. Park, S.-H. Cho, B. J. Kim and I.-D. Kim, *ACS Nano*, 2020, **14**, 11394-11405.
42. W. Zheng, *Analysis & Sensing*, 2023, **3**, e202200070.
43. G. Korotcenkov, *Materials Science and Engineering: B*, 2007, **139**, 1-23.
44. M. Burrows, W. Stockmayer and D. L. Chapman, *Proceedings of the Royal Society of London. Series A. Mathematical and Physical Sciences*, 1940, **176**, 474-483.
45. M. Alaqarbeh, S. F. Adil, T. Ghrear, M. Khan, M. Bouachrine and A. Al-Warthan, *Catalysts*, 2023, **13**, 1343.
46. S. Chen, G. Wang, W. Sui, A. M. Parvez, L. Dai and C. Si, *Industrial Crops and Products*, 2020, **145**, 112164.
47. E. J. Peterson, A. T. DeLaRiva, S. Lin, R. S. Johnson, H. Guo, J. T. Miller, J. Hun Kwak, C. H. F. Peden, B. Kiefer, L. F. Allard, F. H. Ribeiro and A. K. Datye, *Nature Communications*, 2014, **5**, 4885.
48. K. Tang, D. Zeng, F. Lin, Y. Yang and L. Wu, *CrystEngComm*, 2020, **22**, 1251-1260.
49. J. Rymarczyk, E. Czerwosz, R. Diduszko and M. Kozlowski, *Materials Science-Poland*, 2017, **35**.
50. J. I. Avila, R. J. Matelon, R. Trabol, M. Favre, D. Lederman, U. G. Volkmann and A. L. Cabrera, *Journal of Applied Physics*, 2010, **107**.
51. P. M. Gschwend, F. M. Schenk, A. Gogos and S. E. Pratsinis, *Materials*, 2021, **14**, 5921.
52. J. Waser, H. A. Levy and S. Peterson, *Acta Crystallographica*, 1953, **6**, 661-663.
53. A. A. Bolzan, C. Fong, B. J. Kennedy and C. J. Howard, *Acta Crystallographica Section B*, 1997, **53**, 373-380.
54. R. S. Katiyar, P. Dawson, M. M. Hargreave and G. R. Wilkinson, *Journal of Physics C: Solid State Physics*, 1971, **4**, 2421.
55. R. N. Mariammal, K. Ramachandran, B. Renganathan and D. Sastikumar, *Sensors and Actuators B: Chemical*, 2012, **169**, 199-207.
56. C. Chu, D. Huang, S. Gupta, S. Weon, J. Niu, E. Stavitski, C. Muhich and J.-H. Kim, *Nature Communications*, 2021, **12**, 5179.
57. J. Du, Y. Peng, X. Guo, G. Zhang, F. Zhang, X. Fan, W. Peng and Y. Li, *Catalysts*, 2023, **13**, 651.
58. V. V. Kaichev, A. A. Saraev, A. V. Fedorov and E. Y. Gerasimov, *Catalysts*, 2023, **13**, 1435.
59. L. Kuai, Z. Chen, S. Liu, E. Kan, N. Yu, Y. Ren, C. Fang, X. Li, Y. Li and B. Geng, *Nature Communications*, 2020, **11**, 48.
60. H. Liu, J. Fu, H. Li, J. Sun, X. Liu, Y. Qiu, X. Peng, Y. Liu, H. Bao, L. Zhuo, R. Cao, S. Zhang and J. Luo, *Applied Catalysis B: Environmental*, 2022, **306**, 121029.
61. W.-J. Liu, X. Zhou, Y. Min, J.-W. Huang, J.-J. Chen, Y. Wu and H.-Q. Yu, *Advanced Materials*, **n/a**, 2305924.
62. K. Okumura, J. Amano, N. Yasunobu and M. Niwa, *The Journal of Physical Chemistry B*, 2000, **104**, 1050-1057.
63. H. Yan, H. Cheng, H. Yi, Y. Lin, T. Yao, C. Wang, J. Li, S. Wei and J. Lu, *Journal of the American Chemical Society*, 2015, **137**, 10484-10487.
64. J. Zhu, L. Xia, R. Yu, R. Lu, J. Li, R. He, Y. Wu, W. Zhang, X. Hong, W. Chen, Y. Zhao, L. Zhou, L. Mai and Z. Wang, *Journal of the American Chemical Society*, 2022, **144**, 15529-15538.
65. S. Absalan, S. Nasresfahani and M. H. Sheikhi, *Journal of Alloys and Compounds*, 2019, **795**, 79-90.
66. J. Cao, Q. Chen, X. Wang, Q. Zhang, H.-D. Yu, X. Huang and W. Huang, *Research*, 2021, **2021**.
67. A. Kumar, Y. Zhao, M. M. Mohammadi, J. Liu, T. Thundat and M. T. Swihart, *ACS Sensors*, 2022, **7**, 225-234.
68. X.-L. Liu, Y. Zhao, S.-X. Ma, S.-W. Zhu, X.-J. Ning, L. Zhao and J. Zhuang, *ACS Sensors*, 2019, **4**, 3056-3065.
69. R. L. Maynard and R. Waller, in *Air pollution and health*, Elsevier, 1999, pp. 749-796.
70. K. I. Hadjiivanov and G. N. Vayssilov, in *Advances in Catalysis*, Academic Press, 2002, vol. 47, pp. 307-511.
71. V. Muravev, G. Spezzati, Y.-Q. Su, A. Parastaev, F.-K. Chiang, A. Longo, C. Escudero, N. Kosinov and E. J. M. Hensen, *Nature Catalysis*, 2021, **4**, 469-478.
72. G. Spezzati, Y. Su, J. P. Hofmann, A. D. Benavidez, A. T. DeLaRiva, J. McCabe, A. K. Datye and E. J. M. Hensen, *ACS Catalysis*, 2017, **7**, 6887-6891.
73. L. Meng, A.-P. Jia, J.-Q. Lu, L.-F. Luo, W.-X. Huang and M.-F. Luo, *The Journal of Physical Chemistry C*, 2011, **115**, 19789-19796.
74. J. Xu, L. Ouyang, W. Mao, X.-J. Yang, X.-C. Xu, J.-J. Su, T.-Z. Zhuang, H. Li and Y.-F. Han, *ACS Catalysis*, 2012, **2**, 261-269.
75. A. Bensalem, J.-C. Muller, D. Tessier and F. Bozon-Verduraz, *Journal of the Chemical Society, Faraday Transactions*, 1996, **92**, 3233-3237.
76. F. Di Gregorio, L. Bisson, T. Armaroli, C. Verdon, L. Lemaitre and C. Thomazeau, *Applied Catalysis A: General*, 2009, **352**, 50-60.
77. P. P. Dik, O. V. Klimov, I. G. Danilova, K. A. Leonova, V. Y. Pereyma, S. V. Budukva, D. D. Uvarkina, M. O. Kazakov and A. S. Noskov, *Catalysis Today*, 2016, **271**, 154-162.
78. K.-i. Fukui, H. Miyauchi and Y. Iwasawa, *The Journal of Physical Chemistry*, 1996, **100**, 18795-18801.
79. A. J. Hoffman, C. Asokan, N. Gadinas, P. Kravchenko, A. B. Getsoian, P. Christopher and D. Hibbitts, *The Journal of Physical Chemistry C*, 2021, **125**, 19733-19755.
80. M. Ouyang, K. G. Papanikolaou, A. Boubnov, A. S. Hoffman, G. Giannakakis, S. R. Bare, M. Stamatakis, M. Flytzani-Stephanopoulos and E. C. H. Sykes, *Nature Communications*, 2021, **12**, 1549.
81. D. G. Oh, H. A. Aleksandrov, H. Kim, I. Z. Koleva, K. Khivantsev, G. N. Vayssilov and J. H. Kwak, *Molecules*, 2023, **28**, 1957.
82. D. G. Oh, H. A. Aleksandrov, H. Kim, I. Z. Koleva, K. Khivantsev, G. N. Vayssilov and J. H. Kwak, *Molecules*, 2023, **28**.
83. D. Gun Oh, H. A. Aleksandrov, H. Kim, I. Z. Koleva, K. Khivantsev, G. N. Vayssilov and J. Hun Kwak, *Chemistry – A European Journal*, 2022, **28**, e202200684.
84. D. Koziej, N. Bârsan, K. Shimanoe, N. Yamazoe, J. Szuber and U. Weimar, *Sensors and Actuators B: Chemical*, 2006, **118**, 98-104.
85. T. Ghosh, J. M. Arce-Ramos, W. Q. Li, H. Yan, S. W. Chee, A. Genest and U. Mirsaidov, *Nat Commun*, 2022, **13**, 6176.
86. M. Flytzani-Stephanopoulos and B. C. Gates, *Annu Rev Chem Biomol Eng*, 2012, **3**, 545-574.
87. B. C. Gates, A. Katz and J. Liu, *Precision Chemistry*, 2023, **1**, 3-13.
88. D. Zhang, Y. Yang, Z. Xu, D. Wang and C. Du, *Journal of Materials Chemistry A*, 2022, **10**, 10935-10949.

89. K. V. Sopiha, O. I. Malyi, C. Persson and P. Wu, *ACS Appl Mater Interfaces*, 2021, **13**, 33664-33676.
90. H. Zhu, H. Ji, Z. Yuan, Y. Shen, H. Gao and F. Meng, *Journal of Materials Chemistry A*, 2023, **11**, 10565-10576.
91. D. Degler, S. Wicker, U. Weimar and N. Barsan, *The Journal of Physical Chemistry C*, 2015, **119**, 11792-11799.
92. J. Xiang, Y. Su, L. Zhang, S. Hong, Z. Wang, D. Han and F. Gu, *ACS Applied Materials & Interfaces*, 2022, **14**, 13440-13449.
93. P. Li, Z. Wang, Y. Feng, B. Feng, D. Cheng and J. Wei, *Materials Horizons*, 2024, **11**, 3038-3047.
94. D. Jiang, G. Wan, C. E. Garcia-Vargas, L. Li, X. I. Pereira-Hernandez, C. Wang and Y. Wang, *Acs Catalysis*, 2020, **10**, 11356-11364.
95. G. Spezzati, Y. Su, J. P. Hofmann, A. D. Benavidez, A. T. DeLaRiva, J. McCabe, A. K. Datye and E. J. Hensen, *Acs Catalysis*, 2017, **7**, 6887-6891.
96. D. Amalric-Popescu and F. Bozon-Verduraz, *Catalysis today*, 2001, **70**, 139-154.
97. A. Davydov, *Journal of Applied Spectroscopy*, 1992, **56**, 365-371.
98. D. Amalric-Popescu and F. Bozon-Verduraz, *Catalysis Today*, 2001, **70**, 139-154.

† Electronic supplementary information (ESI) available. ICSD 185482. Data retrieved from the Materials Project for PdO (mp-1336) from database version v2023.11.1. For ESI and crystallographic data in CIF or other electronic format see DOI:

Data availability statements

Data retrieved from the Materials Project for PdO (mp-1336) from database version v2023.11.1. Crystallographic data for PdO has been deposited at the ICSD under 185482 and can be obtained from https://www.ccdc.cam.ac.uk/structures/Search?Ccdcid=185482&DatabaseToSearch=ICSD.